A 1-D model for the non-isobaric evaporation of cryogenic liquids in storage tanks

Felipe Huerta[1]*, Ignacio Tapia[1] and Velisa Vesovic[2]

[1]Department of Chemical and Bioprocess Engineering, Pontificia Universidad Católica de Chile

Santiago, Chile

[2]Department of Earth Science and Engineering, Imperial College London,

London SW7 2AZ, United Kingdom

*corresponding author: Tel: (+56) 9 5504 4450, E-mail: fnhuerta@uc.cl

Abstract

A new transient 1-D model relevant to the non-isobaric evaporation of cryogenic liquids has been developed. It provides time-dependent vapour and liquid temperature profiles, tank pressure, liquid volume and evaporation rates. Natural convection in the vapour and liquid phases are simplified to volumetric heat sources that assume instantaneous radial and uniform mixing, respectively. The 1-D model was compared to a CFD model across three experimental scenarios for pressure, vapour temperature and liquid temperature. It was found that the 1-D model achieved a comparable accuracy to CFD, requiring less than $1/1000^{th}$ simulation time. The model can simulate days of evaporation in less than 10 seconds, making it suitable to optimise operating conditions and cryogenic storage tank designs.

1 Introduction

Cryogenic liquids are substances with a saturation temperature below -150 °C at atmospheric pressure. Most cryogenic liquids of industrial interest are formed by liquefaction either of gas mixtures such as air and natural gas, or of pure valuable gases, such as oxygen, methane and hydrogen. Although liquefaction is an energy intensive process [1], the cryogenic liquids have two main benefits that have made their production economically sustainable and socially relevant. At atmospheric pressure, the densities of these liquefied gases are significantly higher than the densities of the gases at room temperature, ranging from 640 kg/m^3 for methane to 871 kg/m^3 for oxygen. This facilitates the storage of these gases in liquefied form, as achieving the same density in the gaseous phase would require extremely high pressures, impractical for industrial supply chains. Secondly, their extremely low temperatures make them suitable refrigerants for industrial processes [2] and efficient energy sinks for cold energy recovery in power cycles [3, 4].

Recently, cryogenic liquids have become pivotal for the sustainable energy transition towards a decarbonised energy landscape. For this purpose, relevant applications are liquid air energy storage (LAES) [5], liquid hydrogen storage [6] and cryogenic CO_2 separation for carbon capture [7]. Although the cryogenic engineering industry is technologically mature, it requires specialised process units to withstand cryogenic temperatures, particularly for the storage of cryogenic liquids. Cryogenic liquids are stored in highly insulated storage tanks to minimise the heat ingress from the surroundings, driven by the large temperature difference between the surroundings and the stored cryogen. As there is no perfect insulation, the heat ingress heats and evaporates the cryogen producing boil-off gas (BOG). The evaporated cryogen accumulates in the vapour phase, increasing the tank pressure. Once the pressure reaches an established set-point, which ranges from 1.1 to 1.3 bar for large scale [8, 9], up to 3.6 bar in mid-scale [10] and up to 10 bar for small scale storage [11], BOG is removed from the tank to reduce the tank pressure.

The continuous generation of BOG creates practical, safety and economic challenges. For large scale storage tanks operating at pressures slightly above the atmospheric, the removed BOG is redirected to a BOG management system for its re-liquefaction or utilisation. In less modern plants and tankers, in extreme scenarios or for small scale storage, the BOG is vented to the atmosphere. The continuous removal of BOG from the storage tank limits the cryogen holding time and limits the economic viability, especially for liquid hydrogen supply chains [6]. Furthermore, it can generate a significant environmental impact in the case of methane or natural gas [12]. Therefore, minimising BOG rates is a key objective in the optimisation of the design and operation of cryogenic storage tanks.

The evaporation and BOG rates during cryogenic liquids storage result from the interplay of complex transport phenomena in both liquid and vapour phases. In particular, natural convection, thermal stratification, self-pressurisation, non-uniform wall heat fluxes to the fluid phases and interfacial heat and momentum transfer all play an important part. The magnitude and relevance of these phenomena depend on the tank scale and operating conditions.

In large-scale tanks, the narrow range of operating pressure results in a nearly isobaric evaporation of the cryogen, where the BOG is continuously removed as it is generated [9, 13, 14]. The isobaric evaporation results in a constant, nearly spatially homogeneous liquid temperature that simplifies liquid-phase transport phenomena. In contrast to the liquid phase, the vapour phase is thermally stratified [15, 16] owing to the interplay of wall heating, natural convection, vapour advection and interfacial cooling [17, 18]. The continuous removal of the generated BOG results in vertical heat advection being a dominant heat transfer mechanism in the vapour phase [17]. The advection governed heat transfer in the vapour phase and the nearly constant, uniform liquid temperature during isobaric-evaporation has enabled the development of reduced-order models [17, 19]. These models have shown a 99% accuracy when validated against CFD simulations [18] and require less than $1/1000^{th}$ of simulation time. This makes them suitable for process and design optimisation.

In small and medium-scale tanks, the pressure operating range is wider than that of large-scale tanks resulting in the non-isobaric storage of the cryogenic liquid. The pressure build-up, owing to liquid evaporation, will continuously increase the saturation temperature of the cryogen, which is equal to the temperature of the vapour-liquid interface. Owing to the low liquid thermal diffusivity, experimental [20-24] and modelling [25-29] research concludes that the interface will heat at a faster rate than the liquid phase bulk. The continuous increase in saturation temperature in conjunction with natural convection induced by the heating of the tank bottom and walls drives liquid thermal stratification. This results in both liquid and vapour thermal stratification, making non-isobaric storage significantly more complex to model than isobaric storage.

In contrast to isobaric storage, reduced order models for non-isobaric storage are scarce and of very limited range of applicability. This has limited progress in the design and optimisation of non-isobaric storage tanks, which are critical for energy storage applications such as liquid hydrogen tanks used in aviation [30] and road freight [31]. Early non-isobaric evaporation models have aimed to provide a physical description of the relevant boundary layers [25, 32] or simplified, but consistent interfacial energy balances [20]. Unfortunately, these models were not able to provide a good prediction of any relevant process variables. More recent models have focused on modelling the interfacial energy

balance by means of effective convection coefficients for the vapour or the liquid or both [23, 33]. These models are simpler than boundary layer models and achieve a better accuracy. However, they neglect liquid thermal stratification and the non-uniform wall heat flux [29]. These models require parameter fitting, which results in a limited range of applicability owing the incomplete description of underlying physics.

Several reduced order models for non-isobaric evaporation model the vapour to interface heat transfer as convective [22, 34, 35]. This approach has two physical limitations. Firstly, all experimental data on vapour thermal stratification [20-24] confirms that the cryogen vapour is a very ineffective medium for heat transfer due to its extremely low thermal conductivity. Secondly, the advective/convective vapour velocities are not only low but circulate the vapour away from the interface in the opposite direction to the vapour-to-interface heat flux [18]. In our previous non-isobaric CFD model [29], we proposed an alternative modelling approach to explain the apparent inconsistency between the measured and modelled vapour and liquid temperature profiles and pressure build-up. The simulations indicate that most of the external vapour heat ingress is conducted through the dry walls to the vapour-liquid interface, producing wall evaporation. This is a result of two effects: (i) the austenitic steel tank wall [36] has a thermal conductivity three orders of magnitude higher than cryogenic vapour and (ii) the small vapour radial temperature gradient at the tank walls [18] decreases the driving force for heat transfer, along the radial direction, in the vapour side of the wall-vapour interface.

In this work, we propose a new one-dimensional model for the non-isobaric evaporation of cryogenic liquid storage tanks with physically sound foundations. The model considers the spatial-temporal variation in the vertical direction of vapour and liquid phases, pressure build-up and wall evaporation. It takes our previous CFD model [30] as the starting point, removing the need to solve the liquid velocity profiles. When compared against the CFD model, the 1-D model achieved an excellent fit in pressure, requiring only a $1/1000^{th}$ of simulation time. This efficiency makes the new model suitable for optimising the design, operation and control of storage tanks, as it simulates hours of evaporation in less than 5 seconds. Simultaneously, its simplicity facilitates the analysis of the transport phenomena that dominate pressurisation and evaporation rates. In Section 2, the physical and mathematical models are described. In Section 3, the model predictions are compared against experimental data and the results obtained with Huerta and Vesovic's CFD model [30] for liquid nitrogen evaporation. In Section 4, a summary and conclusions of the results are given.

2 Model development

2.1 Physical model

The cryogenic storage tank has been modelled as a vertically orientated cylinder with multi layered insulation (MLI) characterised by an effective thermal conductivity. The vapour and liquid have been assumed to be separated by a smooth interface. This assumption is valid for heat fluxes below 50 W m^{-2} K^{-1} typically observed during cryogen storage after the tank has been preconditioned [37, 38]. Figure 1 depicts a schematic of the cryogenic storage tank under non-isobaric conditions. The origin of the coordinate system is set at the bottom of the tank, and the vapour-liquid interface is set at $z = l_{\mathrm{L}}$, where l_{L} is the liquid height. The tank height, H, is constant and equal to $H = l_{\mathrm{L}} + l_{\mathrm{V}}$ where l_{V} is the vapour height. The temperature gradient, between the surrounding air and the cryogen drives several heat ingresses. Namely, heat ingress to the liquid bulk: (i) through the bottom of the tank at a rate $\dot{Q}_{\mathrm{b}}$, (ii) through the tank walls at a rate $\dot{Q}_{\mathrm{L}}$ and (iii) through the vapour-liquid interface at a rate $\dot{Q}_{\mathrm{iL}}$. The vapour phase is heated by heat ingress: (i) through the tank roof at a rate $\dot{Q}_{\mathrm{r}}$ and (ii) through the tank walls at a rate $\dot{Q}_{\mathrm{V}}$, while it is simultaneously cooled by the interphase at a rate $\dot{Q}_{\mathrm{Vi}}$. The wall heat partitioning fraction, η_w, represents the fraction of the external vapour heat ingress $\dot{Q}_{\mathrm{V,ext}}$ that is transferred directly to the vapour-liquid interface [29], primarily by conduction through the tank walls in the negative z-direction. This produces a heat flow to the interface at a rate $\dot{Q}_{\mathrm{V,ext}}\eta_w$ that results in the direct evaporation of the cryogen. As the evaporation progresses, the tank pressure increases owing to the interplay between vapour heating, liquid thermal expansion and phase change.

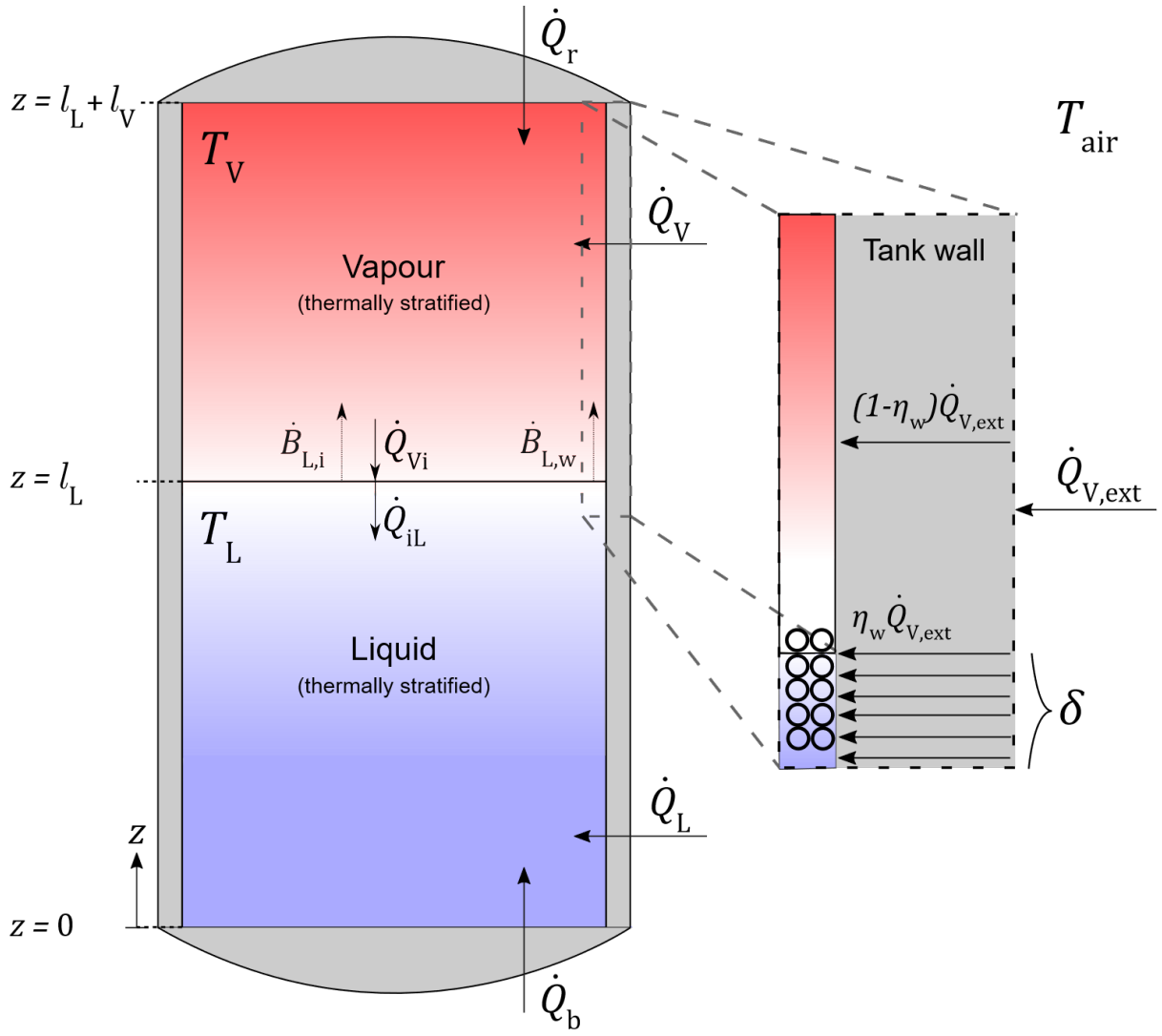


Figure 1: Schematic of the modelled closed cryogenic storage tank. The solid and dashed arrows represent heat and mass flows, respectively. δ is the thickness of the layer below the interface where the η_w fraction of the external vapour heat ingress is transferred to the liquid. The region near the tank wall in contact with the vapour phase and just below the vapour-liquid interface is zoomed-in to illustrate the wall heat flux partitioning.

2.1.1 Vapour phase model

Computational [15, 18, 39] and experimental [20-22, 36] evidence has shown that a steep temperature gradient develops in the vapour phase of cryogens stored in tanks. This indicates that far from the vapour-liquid interface, natural convection and advection in the vertical direction are small and can be neglected. The vapour phase model is the same as in our previous work [29]. Thus, the vapour phase temperature is governed by an unsteady 1-D heat diffusion equation for a compressible gas with a heat source,

$$\frac{\partial T_V}{\partial t} = \bar{\alpha}_V \frac{\partial^2 T_V}{\partial z^2} + \frac{\dot{S}_{w,V}}{\bar{\rho}_V \bar{c}_p} + \dot{S}_c. \quad (1)$$

where T_{V} is the vapour phase temperature, $\bar{\alpha}_{\mathrm{V}} = \bar{k}_{\mathrm{V}}/\bar{\rho}_{\mathrm{V}}\bar{c}_{\mathrm{p}}$ is the vapour thermal diffusivity, and $\overline{\rho}_{\mathrm{V}}$, $\overline{c}_{\mathrm{pV}}$ and $\overline{k}_{\mathrm{V}}$ are the density, specific heat capacity and thermal conductivity, respectively of the vapour phase. The thermophysical properties are evaluated at the average vapour temperature. Therefore, assuming instantaneous radial heat transfer and azimuthal symmetry, the heating of the vapour through the walls is modelled by a volumetric source term,

$$\dot{S}_{\mathrm{w,V}} = \frac{4U_{\mathrm{V}}d_{\mathrm{o}}}{d_{\mathrm{i}}^2}(T_{\mathrm{air}} - T_{\mathrm{V}})(1 - \eta_{\mathrm{w}}), \tag{2}$$

where U_{V} is the overall heat transfer coefficient of the storage tank, d_{o} and d_{i} are the external and internal tank diameters, respectively. The wall heat partitioning fraction is formally defined as,

$$\eta_{\mathrm{w}} = \frac{\int_0^{2\pi}\left(\int_{l_{\mathrm{L}}-\delta}^{l_{\mathrm{L}}} k_{\mathrm{w}}\frac{\partial T_{\mathrm{w}}}{\partial r}|_{r=r_{\mathrm{i}}}dz\right)d\theta}{\dot{Q}_{\mathrm{V,in}}}, \tag{3}$$

where T_{w} and k_{w} are the temperature and the thermal conductivity, respectively of the tank wall. The quantity δ is the height of the region, below the interface, where a large wall heat flux, $\dot{Q}_{\mathrm{V,ext}}\eta_{\mathrm{w}}$, is transferred directly from the tank walls into the cryogenic liquid. As the liquid in this region is close to the saturation temperature, regardless of the level of stratification, this results in its direct evaporation [29]. Recent experimental and modelling evidence suggest that the value of η_{w} is close to unity owing to the rapid vertical heat conduction through the metal part of the wall in contact with the thermally stratified vapour [22, 23, 29]. In this work η_{w} will be either fitted to experimental data for different experimental scenarios or assumed to be equal to 0.97 in other case. This simplifies the need for a full conjugate heat transfer model to compute the wall temperature gradient in the radial direction at the wall-liquid contact line, $\partial T_w/\partial r|_{r=r_{\mathrm{i}}}$.

For large pressurisation rates, the saturation temperature may increase at a faster rate than the temperature of the vapour immediately adjacent to the interface. This will lead to the rapid condensation of vapour in this region. This effect has been modelled by means of a condensation heat source $\dot{S}_{\mathrm{c}}$ [29],

$$\dot{S}_{\mathrm{c}} = \begin{cases} f_{\mathrm{c}}(T_{\mathrm{sat}} - T_{\mathrm{V}}) & \text{if } T_{\mathrm{V}} < T_{\mathrm{sat}} \\ 0 & \text{otherwise} \end{cases}, \tag{4}$$

where f_{c} is a condensation relaxation coefficient. The vapour temperature profile is invariant to f_{c} in the range $10 \leq f_{\mathrm{c}} \leq 3600$, and it can be tuned to improve convergence [29]. Equation 1 is subject to the following initial and boundary conditions,

$$T_{\mathrm{V}}\big(t = 0,\ l_{\mathrm{L}} < z < (l_{\mathrm{L}} + l_{\mathrm{V}})\big) = T_{\mathrm{sat}}(P|_{t=0}), \tag{5.a}$$

$$T_{\mathrm{V}}(z = l_{\mathrm{L}}) = T_{\mathrm{sat}}(P), \tag{5.b}$$

$$k_{\mathrm{V}} \frac{\partial T_{\mathrm{V}}}{\partial z}|_{z=l_{\mathrm{L}}+l_{\mathrm{V}}} = U_{\mathrm{r}}(1-\eta_{\mathrm{w}})(T_{\mathrm{air}} - T_{\mathrm{V}}|_{z=l_{\mathrm{L}}+l_{\mathrm{V}}}). \tag{5.c}$$

where, P is the pressure in the vapour bulk and T_{sat} is the cryogen saturation temperature, which is a function of the pressure. If there is a known heat flux at the tank roof q_{r}, Eq. 5.c is simply $\partial T_{\mathrm{V}}/\partial z|_{z=l_{\mathrm{L}}+l_{\mathrm{V}}} = q_{\mathrm{r}}/k_{\mathrm{V}}$. At the beginning of the evaporation, the vapour temperature is assumed to be equal to the cryogen saturation temperature at the initial pressure (Eq. 5.a). At the vapour liquid interface, the temperature of the vapour is equal to the saturation temperature at the pressure of the vapour (Eq. 5.b) at all times. At the tank roof, the heat flux from the roof to the vapour is driven by the temperature difference between the surroundings and the vapour in contact with the tank roof (Eq. 5.c).

2.1.2 Liquid phase model

The evaporation of the cryogenic liquid and the heating of its vapour will increase the tank pressure and consequently increase the cryogen saturation temperature. Because of the low liquid thermal diffusivity, the saturation temperature will increase faster than the bulk temperature, inducing thermal stratification [20-23, 36, 40, 41]. The thermally stratified layer will develop vertically from the interface towards the bottom of the tank. It is worth noting that thermal stratification will dampen natural convection in the thermally stratified layer [18, 29]. Therefore, it will be assumed that the thermal boundary layer will develop at the rate corresponding to the physical time scale of thermal diffusion, $\delta \propto \sqrt{4\bar{\alpha}_{\mathrm{L}} t}$, where $\bar{\alpha}_{\mathrm{L}}$ is the liquid thermal diffusivity evaluated at the average liquid temperature and *t* is the time. On this basis, advection will be neglected. Far from the interface, the liquid is mixed radially by buoyancy driven flows originated at the regions adjacent to the heated bottom and tank walls [29]. These are modelled as two volumetric source terms that indicate the different levels of mixing due to the heating of the liquid by the tank bottom, $\dot{S}_{\mathrm{b}}$, and by the tank walls, $\dot{S}_{\mathrm{w}}$. This results in an unsteady, 1-D heat diffusion equation with two source terms,

$$\frac{\partial T_{\mathrm{L}}}{\partial t} = \bar{\alpha}_{\mathrm{L}} \frac{\partial^2 T_{\mathrm{L}}}{\partial z^2} + \frac{1}{\bar{\rho}_{\mathrm{L}} \bar{c}_{\mathrm{p}}} (\dot{S}_{\mathrm{w}} + \dot{S}_{\mathrm{b}}), \tag{6}$$

where T_{L} is the liquid phase temperature. The wall and bottom heating source terms are defined as,

$$\dot{S}_{\mathrm{w}} = \frac{4U_{\mathrm{L}} d_{\mathrm{o}}}{d_{\mathrm{i}}^2} (T_{\mathrm{L}} - T_{\mathrm{air}}), \tag{7}$$

$$\dot{S}_{\mathrm{b}} = \frac{U_{\mathrm{b}}(T_{\mathrm{L}}|_{z=0} - T_{\mathrm{air}})}{l_{\mathrm{L}}}. \tag{8}$$

where U_{L} and U_{b} are the overall heat transfer coefficients of the tank walls and tank bottom, respectively. These coefficients are allowed to differ, as in some cryogen storage scenarios, the heat flux through the bottom of the tank is higher than through the tank walls. In those scenarios, the bottom of the tank is either heated to prevent ground freezing or supported by pillars that conduct heat from the ground. Eq. 6 is subject to the following initial and boundary conditions,

$$T_{\mathrm{L}}|_{t=0} = T_{\mathrm{sat}}(P_0), \tag{9.a}$$

$$T_{\mathrm{L}}|_{z=l_L} = T_{\mathrm{sat}}(P), \tag{9.b}$$

$$\frac{\partial T_{\mathrm{L}}}{\partial z}|_{z=0} = 0. \tag{9.c}$$

These boundary conditions indicate that: (i) at the beginning of the evaporation, the liquid temperature is spatially homogeneous and equal to the saturation temperature at the initial pressure (Eq. 9.a); (ii) at the vapour-liquid interface, the liquid temperature is equal to the saturation temperature at the given vapour pressure (Eq. 9.b) and (iii) as the bottom heat ingress is included as a volumetric source term, see Eq. 8, a zero gradient boundary condition is set at the tank bottom (Eq. 9.c) to avoid double-counting the bottom heat ingress. Equations 9.a-9.c constitute an initial-boundary value problem (IBVP) for the liquid phase.

2.1.3 Evaporation rate and pressure evolution

The evaporation rate $\dot{B}_{\mathrm{L}}$ is modelled as the sum of interfacial evaporation and the direct evaporation due to the wall heat conduction, $\dot{Q}_{\mathrm{V,ext}}\eta_{\mathrm{w}}$, [29],

$$\dot{B}_{\mathrm{L}} = \dot{B}_{\mathrm{L,i}} + \dot{B}_{\mathrm{L,w}}. \tag{10}$$

The interfacial evaporation is defined by means of the energy balance at the vapour-liquid interface, using the Fourier's law,

$$\dot{B}_{\mathrm{L,i}} = \frac{k_{\mathrm{V}}\frac{\partial T_{\mathrm{V}}}{\partial z}|_{z=l_L^+} - k_{\mathrm{L}}\frac{\partial T_{\mathrm{L}}}{\partial z}|_{z=l_L^-}}{\Delta H_{\mathrm{LV}}}, \tag{11}$$

where ΔH_{LV} is the latent heat of vaporisation of the stored cryogen. The spatial positions defined by $z = l_{\mathrm{L}}^+, z = l_{\mathrm{L}}^-$ represent the region just above and just below the vapour-liquid interface. Adjacent to the

fluid-wall contact line, the wall heat flux is amplified by two distinct mechanisms. First, far from the interface, the dampening of natural convection and low thermal conductivity induce thermal stratification in both fluid phases. This stratification is more pronounced in the vapour phase [18] than in the liquid phase [29], leading to a less efficient heating effect of the wall in contact with the liquid phase. Second, evaporation near the wall instigates a minor convective loop that circulates from the interface towards the centre of the tank before returning to the wall [29]. This results in a non-uniform vertical distribution of wall heat flux [42, 43], where a substantial portion of heat flux is directly transferred from the wall to the liquid just beneath the vapour-liquid interface. The interaction between these mechanisms and the high thermal conductivity of the wall in the z-direction culminates in a significant proportion of external heat ingress into the vapour being transferred directly downwards through the metal part of the wall to the interface. The heat directly transferred to the interface induces evaporation, defined as the wall evaporation, at the rate,

$$\dot{B}_{\mathrm{L,w}} = \frac{\eta_{\mathrm{w}} \dot{Q}_{\mathrm{V,ext.}}}{\Delta H_{\mathrm{LV}}}, \tag{12}$$

The mass balance over the vapour subsystem results in,

$$\bar{\rho}_{\mathrm{V}} \frac{\partial V_{\mathrm{V}}}{\partial t} + V_{\mathrm{V}} \frac{\partial \bar{\rho}_{\mathrm{V}}}{\partial t} = \dot{B}_{\mathrm{L}}, \tag{13}$$

where V_{V} is the vapour volume. As the tank volume is constant, the liquid volume can be calculated directly from,

$$V_{\mathrm{L}} = V_{\mathrm{T}} - V_{\mathrm{V}}, \tag{14}$$

where V_{T} is the tank volume. The total mass of stored cryogen is constant over time and equal to,

$$m_{\mathrm{tot}} = V_{\mathrm{T}}\left(\bar{\rho}_{\mathrm{L}} LF + \bar{\rho}_{\mathrm{V}}(1 - LF)\right), \tag{15}$$

where *LF* is liquid filling defined as, $LF = V_{\mathrm{L}}/V_{\mathrm{T}}$. The pressure in the vapour is evaluated using an equation of state,

$$P = \bar{\rho}_{\mathrm{V}} \bar{Z}_{\mathrm{V}}(P, \bar{T}_V) R \bar{T}_{\mathrm{V}}, \tag{16}$$

where $\bar{T}_{\mathrm{V}} = 1/l_{\mathrm{V}} \int_0^{l_{\mathrm{V}}} T_{\mathrm{V}} dz$ is the average vapour temperature, and the vapour phase compressibility factor, $\bar{Z}_{\mathrm{V}}$, is evaluated at the pressure and average vapour temperature of the cryogen.

2.2 Computational implementation

The non-isobaric evaporation model has been implemented in MATLAB R2023b®. The partial differential equations, alongside their initial and boundary conditions for the vapour and liquid sub-models, were discretised explicitly in space using the method of lines [44]. The second-order spatial derivatives were discretised using second-order central approximations to ensure a second-order accuracy of the solution. The Robin boundary conditions for the vapour and liquid subsystems were discretised using second-order backward and forward differences for the first derivative, respectively. A grid spacing of $\Delta z = 1$ mm was required to ensure grid independence, producing grids with $n_{z\mathrm{L}} = l_L/\Delta z + 1$ computational nodes in the liquid and $n_{z\mathrm{V}} = l_\mathrm{V}/\Delta z + 1$ nodes in the vapour. The explicit discretisation of the PDEs and their boundary conditions produced a system of $n_{z\mathrm{L}} + n_{z\mathrm{V}}$ ordinary differential equations. This system was augmented with the mass balance in Eq. (13) and the non-linear thermodynamic equilibrium equation, Eq. (16), producing a differential-algebraic equations (DAE) system. The DAE system was integrated using the highly efficient ode15i variable-step, variable-order routine [45] to minimise simulation time while retaining a high numerical accuracy. For each equation, the convergence criterion has been established by setting the absolute and relative tolerances to 10^{-9} and 10^{-4}, respectively. Although the convergence criteria were strict, the convergence was very fast. The simulation of 2 hours of non-isobaric evaporation took less than 10 s in a single core of an Intel® Core™ i5-7300HQ CPU processor.

3 Results

The 1-D model was validated against Kang et al. [21] experimental data for non-isobaric evaporation of liquid nitrogen (LN_2). The experiments were carried out over intermediate heat fluxes (18-65 Wm^{-2}), resulting in a broad pressure range (0.1–1 MPa). These conditions represent a stringent test, which allows for the identification of the range of applicability of the developed model.

The Kang et al. [21] experimental set-up was not fully characterized, so a number of model parameters were obtained by fitting to the available measurements. In particular, the overall heat transfer coefficients for vapour and liquid and the wall heat partitioning factor were treated as adjustable parameters. The fitting procedure used the measured pressure, liquid and vapour temperatures for this purpose. The necessity of using three fitting parameters arises primarily to take into consideration, in a simplified manner, the non-unform heat flux distribution in the internal tank wall [29]. A detailed description of the parameter fitting strategy to is presented in Supplementary Material SM1.The vapour temperature initial condition was a third-degree polynomial fitted to the measured vapour temperature profile at the beginning of the experiments. The overall heat transfer coefficient for the bottom of the tank was calculated from the experimentally available heat flux, as $U_{\mathrm{b}} = q_{\mathrm{b,exp}}/(T_{\mathrm{air}} - T_{\mathrm{L}})$. The roof was assumed thermally insulated, $q_{\mathrm{r}} = 0$, in agreement with the results of finite element analysis performed by Kang et al. for their experimental configuration [21]. Nitrogen was assumed to behave as an ideal gas, $\bar{Z}_{\mathrm{V}} = 1$, as this retained the simplicity of the model. More complex equations of state that were tested did not improve the fit. The values of fitted parameters are given in Table 1. As the 1-D model has a simplified representation of liquid phase heat transfer, the fitted parameters differ from those obtained when fitting the CFD model. The fitted values for the overall heat transfer coefficients are within the order of magnitude of values used for cryogen storage tanks. For example, the large-scale LNG tank used by Migliore et al. was characterised by the coefficients $U_{\mathrm{L}} = U_{\mathrm{V}} = 0.36$ $Wm^{-2}K^{-1}$ [9]. In a separate study, the lab-scale LN_2 tank used by Perez et al. was characterised by the coefficients $U_L = 0.25\ Wm^{-2}K^{-1}, U_V = 0.24\ Wm^{-2}K^{-1}$) [22].

Table 1: Fitted parameters for the 1-D and CFD models for Kang et al. [21] experiments of LN2 evaporation in a 10 L vertically orientated storage tank. The overall heat transfer coefficients at the tank bottom, U_{b}, were available in the experimental data and equal to 2.71, 2.73 and 3.12 W $m^{-2}K^{-1}$ for the liquid fillings of 0.3, 0.5 and 0.8, respectively.

	LF = 0.3		LF = 0.5		LF = 0.8	
Parameter	1-D	CFD	1-D	CFD	1-D	CFD
η_w	0.914	0.970	0.949	0.980	0.959	0.980
U_{L} (W m^{-2} K^{-1})	0.347	0.220	0.365	0.300	0.299	0.210
U_{V} (W m^{-2} K^{-1})	0.088	0.130	0.138	0.190	0.214	0.420

The thermodynamic and thermophysical properties of nitrogen are calculated using a Helmholtz-energy-explicit-type multiparameter equation of state [46] part of the open-source library COOLPROP [47]. The saturation temperature was calculated using Antoine's equation.

3.1 Comparison of 1-D model and CFD model against experimental data

In this section, the pressure build-up and temperature profiles obtained with the 1-D model are compared to experimental data and to the predictions of our CFD model [29]. Figure 2 shows the variation of vapour pressure as a function of time for three different liquid filling scenarios measured by Kang et al. in their LN_2 non-isobaric evaporation experiments [21]. Low (LF = 0.30), intermediate (LF = 0.50) and high (LF = 0.80) liquid fillings are depicted in yellow, mustard and blue colours, respectively. Experimental data is shown as circles, while the 1-D and CFD model's predictions are shown as solid and dashed lines, respectively. In general, we would expect the CFD model to fit the experimental data better than the 1-D model. However, a complete convergence of the parameter fitting requires roughly a thousand evaluations of the objective function. With the CFD model, each evaluation required between 1 and 2 hours, compared to 5 s with the 1-D model. Hence, the computational constraints resulted in the CFD effective parameters being of lower accuracy than those of the 1-D model.

For high LF scenarios, the 1-D model achieved an excellent agreement. The average absolute deviation (AAD) and maximum percentage deviation (MD) between the predicted and experimental pressures were 1.7% and 1.8%, respectively. The deviations are smaller than those obtained with the CFD model. For low and intermediate liquid fillings, the agreement was adequate (AAD = 6.3%, MD = 30.8%) and similar to the CFD model. For all scenarios, the 1-D model slightly overpredicts the pressurisation rate at the beginning of the evaporation. As the evaporation progresses and the pressure increases, the overprediction decreases until the trend reverses at higher times. Towards the end of the evaporation and as the pressure approaches 1 MPa, the 1-D model underpredicts the pressurisation. To understand the causes of these deviations, we turn our attention to the temperature profiles.

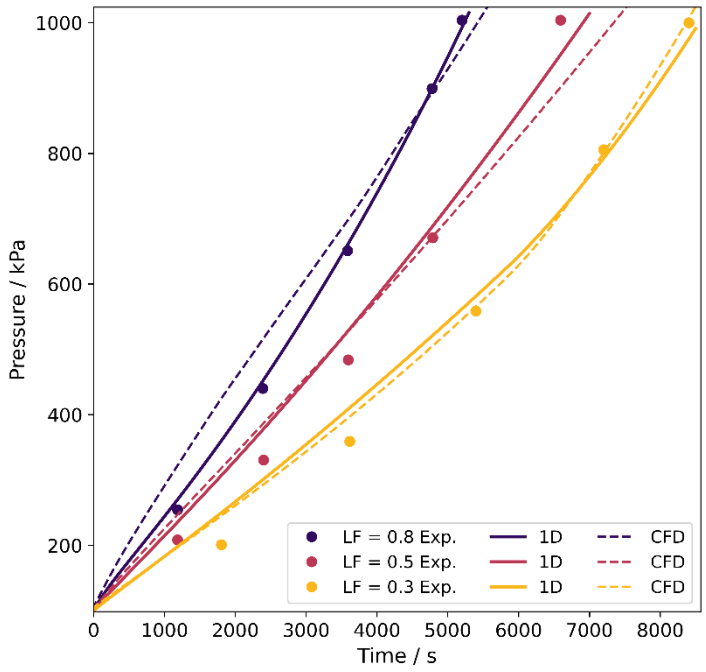


Figure 2: Comparison of the pressure variation during the non-isobaric evaporation of LN_2 in a vertically-oriented 10 L storage tank between the experimental data of Kang et al. [21] and the predictions of the two models: experimental data (circles), 1-D (solid lines) and CFD (dashed lines); Low (LF = 0.3), intermediate (LF = 0.5) and high (LF = 0.8) liquid fillings are depicted in yellow, crimson red and dark blue, respectively.

Figure 3 shows the vapour temperature profiles obtained with the 1-D and CFD models for low (Fig. 3a), intermediate (Fig. 3b) and high (Fig. 3c) liquid fillings, respectively. The abscissa represents the vapour temperature, and the ordinate represents the vertical distance from the interface. The initial temperature profile is depicted in black, and the following time steps are depicted in colours that increase their light intensity until yellow is depicted to represent the end of the simulation. The line-style convention for 1-D, CFD and experiments is the same as that used in Fig. 2. For all scenarios and time steps, the 1-D model achieves an excellent agreement in reproducing the vapour temperature (AAD < 1.2%, MD < 3.6%). The CFD model predicts very similar profiles as both models share the same vapour phase sub-model. The small differences can be attributed to differences in the interfacial temperature owing to the differences in predicted pressures, see Figure 2.

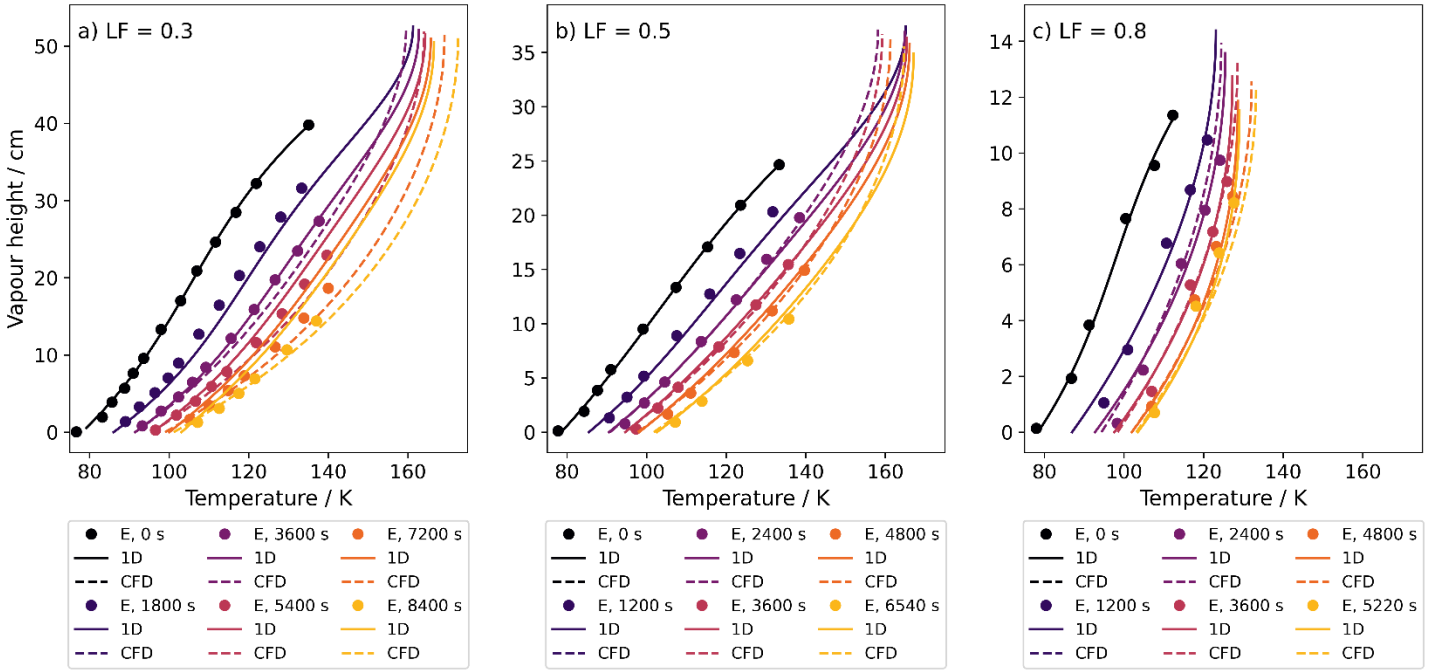


Figure 3: Comparison of the vapour temperature variation during the non-isobaric evaporation of LN_2 in a vertically-oriented 10 L storage tank between the experimental data of Kang et al. [21] and the predictions of the two models: experimental data (circles, E), 1-D (solid lines) and CFD (dashed lines). Subfigures a, b and c show low (LF = 0.3), intermediate (LF = 0.5), and high (LF = 0.8) liquid fillings, respectively. In each subfigure, the y-axis shows the vertical distance from the vapour-liquid interface, while the x-axis shows the vapour temperature.

Figure 4 compares the liquid temperature profiles obtained with the 1-D and CFD models against Kang et al. [21] experiments for low (4a), intermediate (4b) and high (4c) liquid fillings, respectively. The abscissa represents the liquid temperature, and the ordinate represents the vertical distance from the bottom of the tank. The colour and line-style conventions are the same as those in Figure 3. As evaporation progresses, the temperature of the liquid increases and thermal expansion, rather than evaporation, dominates the liquid volume change. This leads to an increase in a liquid volume and the upward displacement of the vapour-liquid interface, as can be observed in Figs 3 and 4. Overall, the liquid temperature predicted by the 1-D model is in good agreement with experimental data for all scenarios (AAD < 1.1%, MD < 5.6%).

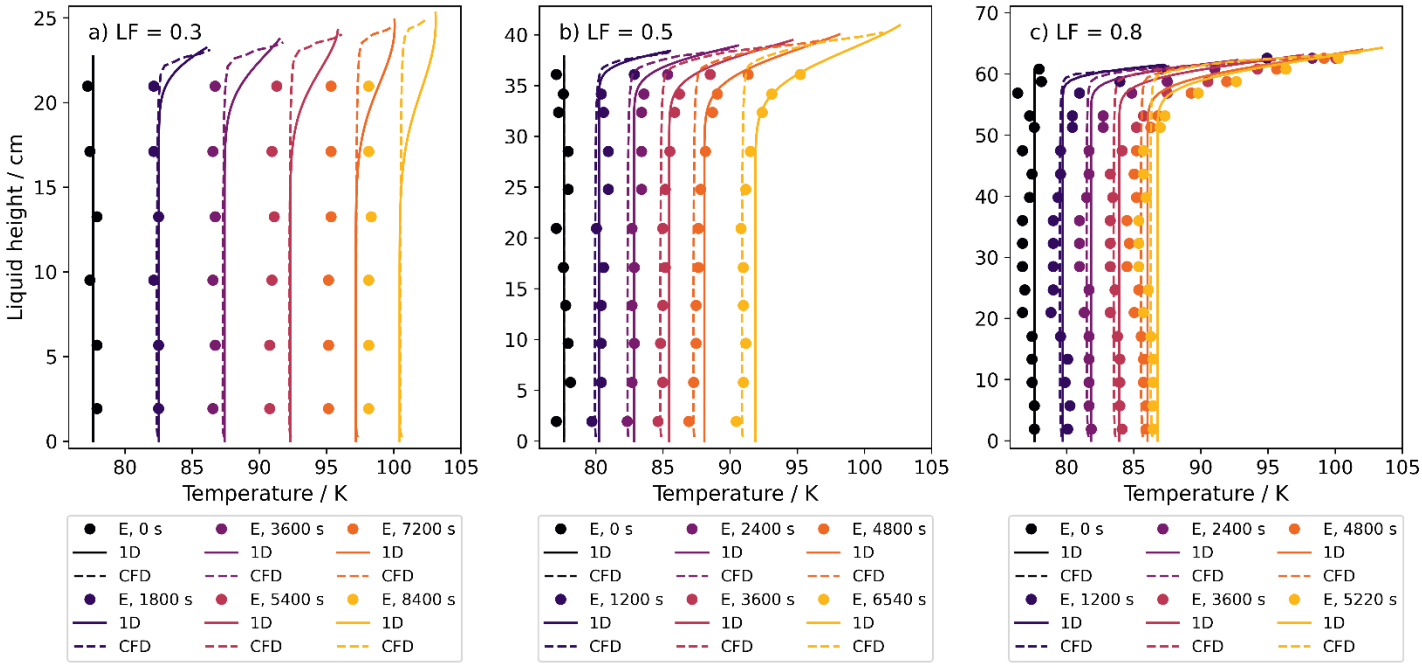


Figure 4: Comparison of the liquid temperature variation during the non-isobaric evaporation of LN_2 in a vertically-oriented 10 L storage tank between the experimental data of Kang et al. [21] and the predictions of the two models: experimental data (circles, E), 1-D (solid lines) and CFD (dashed lines) Subfigures a, b and c show low (LF = 0.3), intermediate (LF = 0.5), and high (LF = 0.8) liquid fillings, respectively. In each subfigure, the y-axis shows the vertical distance from the bottom of the tank, while the x-axis shows the liquid temperature.

The main differences between the experimental temperature profiles and the 1-D model predictions are observed immediately below the vapour-liquid interface, see Figure 4. The 1-D model does not accurately reproduce the temperature profile in the region below the interface for low and high liquid fillings. For low liquid filling, the 1-D model overpredicts the liquid temperature and shows an S-shaped temperature profile, see Fig. 4a. The S-shape would require that the maximum resistance to heat transfer occurs in an intermediate region between the interface and liquid bulk. This has not been observed in any of the most relevant experimental studies for non-isobaric cryogen evaporation [20, 22, 36, 48]. In contrast, those studies show a concave profile characteristic of a boundary layer in the presence of natural convection, qualitatively similar to that obtained by the CFD model, see the dashed lines in Fig. 4a. For high liquid filling, the 1-D model predicts a temperature profile that propagates through the region equal to the physical length scale of heat conduction, $\delta \sim 4\sqrt{\bar{\alpha}_L t}$. In contrast, the experimental data exhibits a temperature boundary layer that propagates instantly, see Fig. 4c. The size of this region is a result of convective currents below the interface, which are stronger in the high liquid filling scenarios than in other scenarios. In conclusion, the differences in liquid temperature near the interface predicted by the 1-D model and experimental data arise from neglecting advection and simplifying natural convection, see Eq. 6.

The pressure build-up is governed by cryogen evaporation, liquid thermal expansion and vapour heating. Figures 3 and 4 show that the predictions of the 1-D model are in good agreement with measured vapour temperature profiles and with the bulk liquid temperature. Therefore, we can surmise that the deviations observed for the pressure build-up, see Figure 2, can be attributed to inaccuracies in the evaporation rate. The 1-D model underprediction of the liquid temperature gradient below the interface, see Figure 4, implies an underprediction of the interfacial cooling by the liquid, see Eq. 11. To compensate for this effect, the parameter fitting procedure decreases the wall heat partitioning coefficient, η_{w}, and the vapour phase heat transfer coefficient, U_{V}, see Table 1. This results in an overestimation of the initial evaporation rate, owing to the underprediction of interfacial cooling, and an underestimation of the long-term evaporation rate, owing to the underestimation of the wall evaporation, see Eq. 12. The former results in the overprediction of the pressure build-up during the initial stages, while the latter results in the underpredictions of the pressures, as can be seen in Figure 2.

Notwithstanding the minor deviations discussed so far, overall, the good fit achieved for pressure, liquid and vapour temperatures demonstrates the usefulness of the 1-D model for practical applications.

3.2 *Comparison between 1-D and CFD models using best-fit CFD parameters*

In this section, the assumptions of the 1-D model are tested by comparison them to those of the CFD model. For this purpose, we run both models using the CFD parameters, see Table 1. Figure 5 shows the pressure build-up predicted by the CFD and 1-D models using the same parameters. The 1-D model significantly overpredicts the pressure in both scenarios, showing a larger overprediction for large liquid filling. This pressure overprediction resulted from the 1-D model overprediction of the evaporation rate, see Eq. (10), which was the main driver of pressure build-up. On average, the 1-D model overpredicted the evaporation rate by 70-90%. In contrast, the wall evaporation, see Eq. 12, was comparable in both models. The largest difference observed was 17% higher in the 1-D model for the low liquid filling scenario.

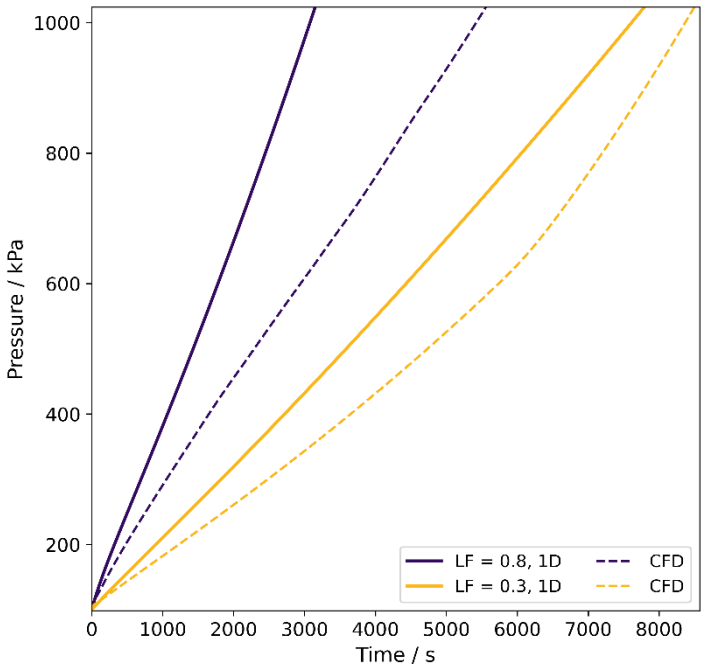


Figure 5: Comparison of the pressure variation during the non-isobaric evaporation of LN_2 in a 10 L vertically-oriented storage tank between the 1-D (solid lines) and CFD (dashed lines) models. Low (LF = 0.3) and high (LF = 0.8) liquid fillings are depicted in yellow, and blue, respectively.

As the 1-D model does not resolve natural convection, it underestimates the liquid temperature gradient below the interface, $\partial T_{\mathrm{L}}/\partial z|_{z=l_L^-}$. The underestimation of the liquid vertical temperature below the interface results in an underestimation of the interfacial cooling. This underestimation is higher for large liquid filling owing to more vigorous natural convection [29]. The interfacial cooling term, see Eq. 11, dominated the interfacial energy balance in all scenarios, which resulted in a negative interfacial evaporation rate $\dot{B}_{\mathrm{L,i}}$ that signalled the presence of interfacial condensation. However, the evaporation

rate, $\dot{B}_{\mathrm{L}}$, calculated by both CFD and 1-D models was positive for all scenarios because wall evaporation, $\dot{B}_{\mathrm{L,w}}$, dominated over interfacial condensation. Therefore, in the 1-D model, the higher evaporation rates, $\dot{B}_{\mathrm{L}}$, that produced faster pressurisation, see Figure 5, resulted from the significantly lower interfacial condensation rate.

Figure 6a shows the liquid temperature profile for the scenarios of low (LF = 0.3) and high (LF = 0.8) liquid fillings in yellow and black lines, respectively. Dotted lines are used to illustrate the initial vapour temperature, while the vapour temperature profiles at the end of the simulation are depicted as solid and dashed lines for the 1-D and CFD models, respectively. Two y-axes are displayed for the liquid height: (i) in black, on the left-hand side, for high liquid filling and (ii) in yellow, on the right-hand side, for low liquid filling. Figure 6b shows the differences between the predictions of the 1-D and CFD models for average liquid and interfacial temperature in dotted and solid lines, respectively, for low and high liquid fillings. For both liquid fillings, the 1-D model overpredicted the interfacial temperature and underpredicted the average liquid temperature, see Figs. 6a-b. The higher interfacial temperature predicted by the 1-D model is a consequence of the pressure overprediction, see Figure 5, as pressure determines the saturation temperature that is used as a boundary condition at the vapour-liquid interface. Consequently, the larger interfacial temperature overprediction for high liquid filling, compared with low liquid filling, results from the larger pressure overprediction for this liquid filling, see Figure 5.

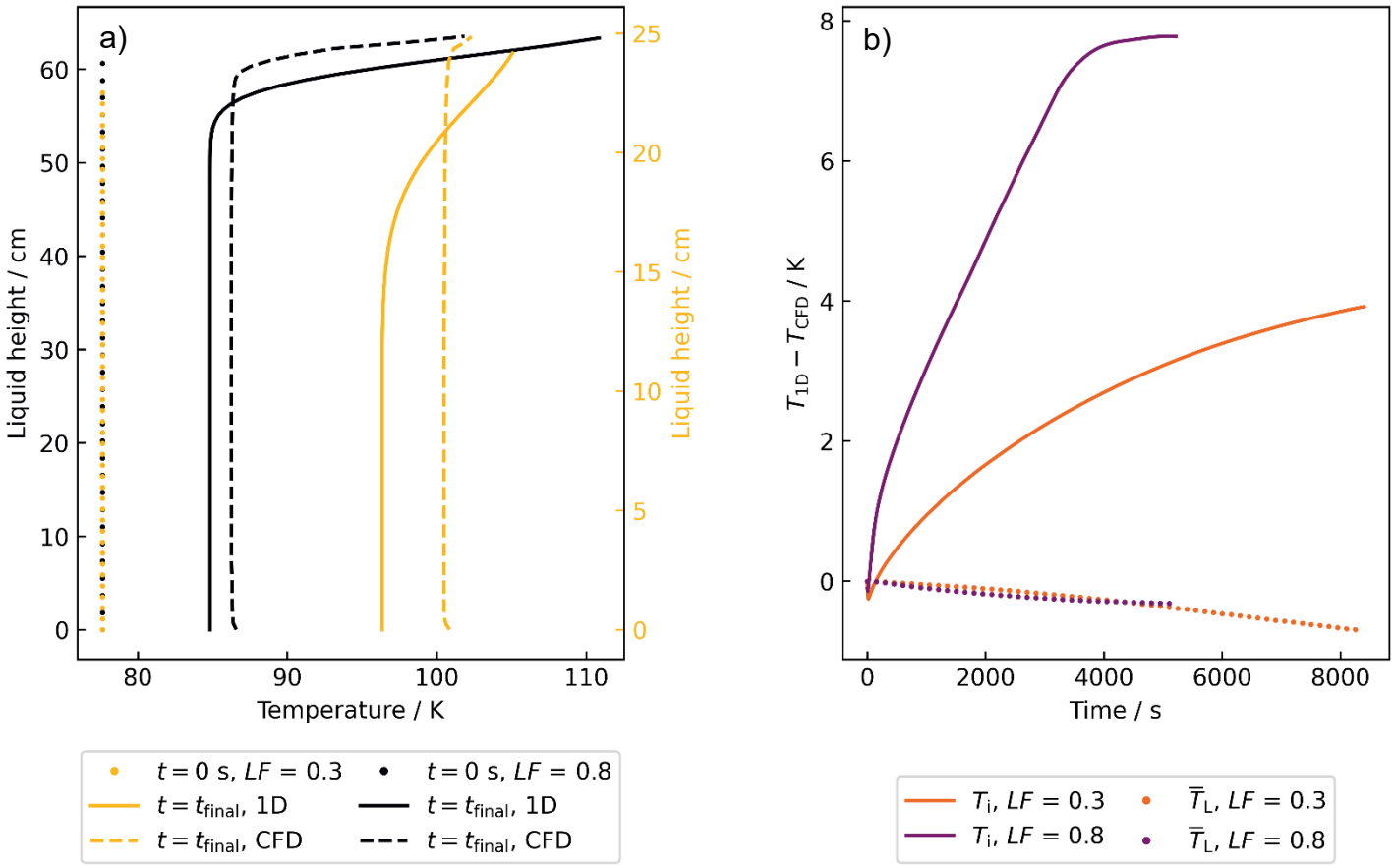


Figure 6: Comparison of the liquid temperature variation during the non-isobaric evaporation of LN_2 in a 10 L vertically-oriented storage tank between the 1-D and CFD models. Subfigure (a) shows the liquid temperature profiles at the end of each simulation for the 1-D model in solid lines and the CFD model in dashed lines for low (LF = 0.30) and high (LF = 0.80) liquid fillings. The initial temperature profile of each scenario is depicted in dotted lines. Subfigure (b) shows the difference between the interfacial (--) and average (..) liquid temperatures predicted by the 1-D and CFD models for each liquid filling.

The lower average liquid temperature predicted by the 1-D model, see Figure 6b, results from the differences in the macroscopic energy balance of the liquid phase. The simulations indicate that the difference can be attributed to the interfacial cooling term in Eq. 11 as the bottom and wall heat ingresses differed by less than 1% between the two models. The interfacial cooling flux by the interface is governed by the liquid temperature gradient below the interface, which was significantly smaller in the 1-D model. This resulted in the 1-D model underpredicting interfacial liquid heating and consequently the average liquid temperature.

Figure 7a shows the vapour temperature profiles at the beginning and the end of the evaporation for low and high liquid fillings following the same colour and line-style conventions as that of Figure 6a. Although the shape of the temperature profiles, by the end of the experiment, are qualitatively similar, the quantitative agreement is poor with the 1-D model underpredicting the vapour temperature over

most of the domain. The larger differences observed for the lower filling can be partially attributed to the longer experimental run.

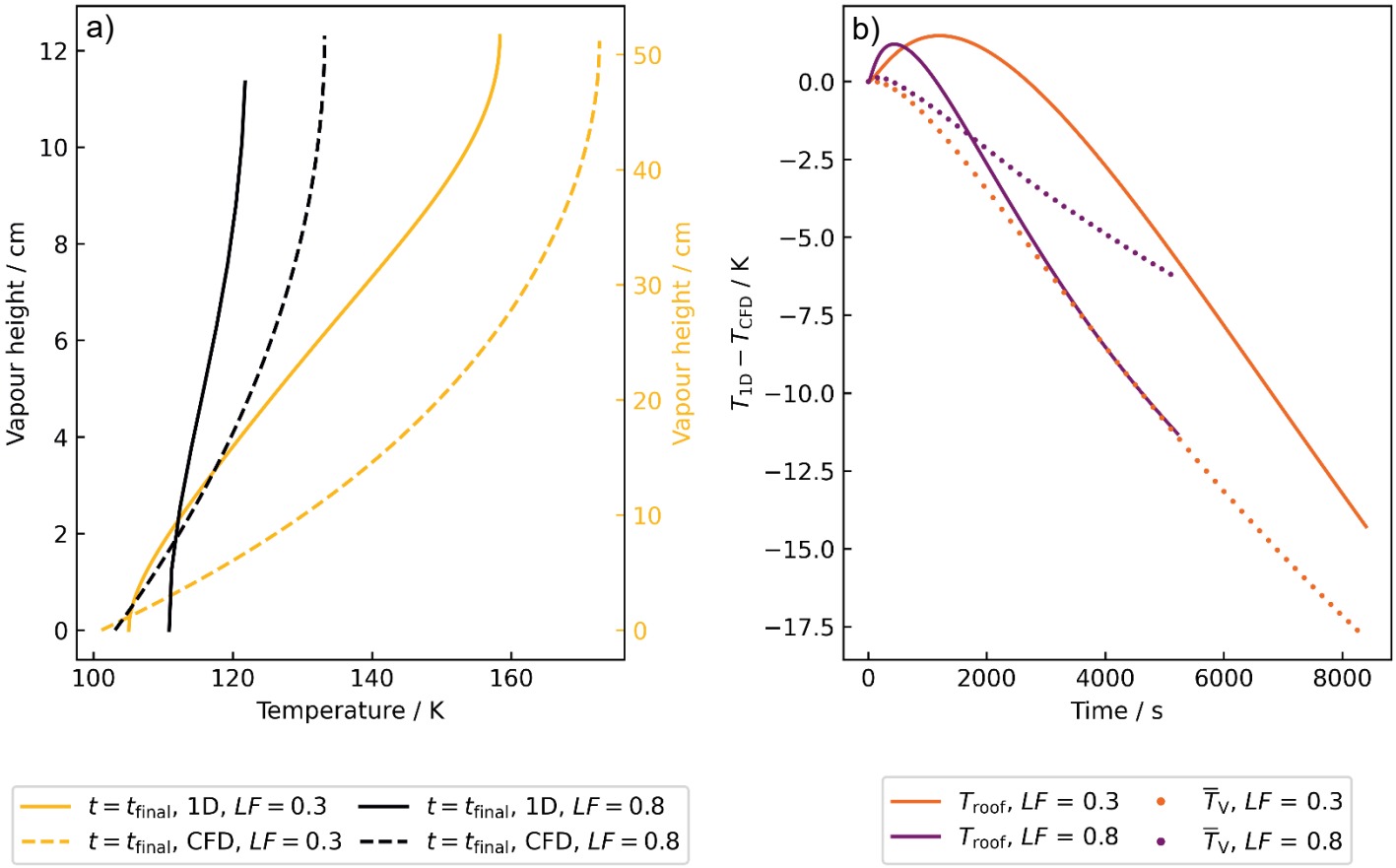


Figure 7: Comparison of the vapour temperature variation during the non-isobaric evaporation of LN_2 in a 10 L vertically orientated storage tank between the 1-D and CFD models. The parameters used in both models were obtained through parameter fitting of the CFD model to Kang et al. [21] experiments. Subfigure (a) shows the vapour temperature profiles at the end of each simulation for the 1-D model in solid lines and the CFD model in dashed lines for low (LF = 0.30) and high (LF = 0.80) liquid fillings. Subfigure (b) shows the difference between the roof (--) and average (..) vapour temperatures predicted by the 1-D and CFD models for each liquid filling.

Figure 7b shows the difference between the predictions of the 1-D and CFD models of average vapour temperature following the same colour and line-style contentions as that of Figure 6b. For both liquid fillings, the 1-D model underpredicts the average vapour temperature, and the deviations increase in magnitude monotonically with time. For the roof temperature, the 1-D model first overpredicts and then monotonically underpredicts the roof temperature for both liquid fillings.

The differences in vapour temperature can be attributed to the higher evaporation rates, resulting in higher pressure and higher vapour density in the 1-D model. In essence, the higher overall pressure predicted by the 1-D model resulted in 25% (LF = 0.30) and 67% (LF = 0.80) higher vapour densities at the end of the simulation compared to the CFD model. As we are dealing with a compressible gas,

changes in pressure, rather than in temperature, dominate changes in density. The significantly higher vapour densities were observed in conjunction with vapour volumes, which were only 2% different. This yielded a larger vapour mass in the 1-D model. Heating a larger mass of vapour will result in a lower vapour temperature, for the same heating rate. Simultaneously, a lower vapour temperature produces an increase in driving force, $T_{\mathrm{air}} - T_{\mathrm{V}}$, see Eq. 2. The simulations indicate that the contribution of the former is higher (25.4% for LF = 0.30 and 73.5% for LF = 0.80) than that of the latter (6.6% for LF = 0.30 and 1.8% for LF = 0.80). This interplay between the two effects explains the underprediction of average vapour temperature by the 1-D model.

The initial overprediction and subsequent underprediction of roof temperature is a consequence of the differences in the transient evolution of vapour temperatures. Eq. 1 is the superposition of unsteady heat conduction, linking the vapour bulk temperature to the temperature of the interface and the roof, and to the wall heating. The physical time scale for heat conduction is $\tau \sim l_{\mathrm{V}}^2/\bar{\alpha}_{\mathrm{V}} = \bar{\rho}_{\mathrm{V}} l_{\mathrm{V}}^2/(\bar{k}_{\mathrm{V}}\bar{c}_{\mathrm{p}})$. During the initial overprediction period, the roof temperature predicted by the 1-D model was less than 1 K higher than the CFD model. Therefore, the changes in average vapour thermal conductivity or heat capacity between the two models in that period are negligible. In contrast, the time-averaged vapour density obtained with the 1-D model during this period is 15% and 32% higher for low and high liquid filling, respectively. As the vapour volumes differed by less than 2%, the vapour heights l_{V} in both models are comparable and $\tau_{\mathrm{1D}}/\tau_{\mathrm{CFD}} \sim \bar{\rho}_{\mathrm{V,1D}}/\bar{\rho}_{\mathrm{V,CFD}} > 1$. This implies that the roof perceives the interfacial cooling at a later time in the 1-D model, resulting in a higher temperature. The roof temperature is also influenced by wall heating. The smaller wall heating contribution for the 1-D model, compared with the CFD model, leads to lower roof temperature. In the initial stages, the lack of interfacial cooling is main contributor, and we observe 1-D model overpredicting the roof temperature. At later stages, the effects of interfacial cooling are felt, and together with smaller wall heating contribution, results in the temperature maximum observed in Fig 7b. From this point onwards, the difference in the roof temperature dynamics is analogous to the difference in the average vapour temperature, as they both increase monotonically. The appearance of the maximum temperature at later times for the low liquid filling scenario compared to the high liquid filling scenario is a direct consequence of 3.5 times larger vapour height, which delays the cooling effect of the interface.

An additional comparison between 1-D and CFD models was performed using Seo and Jeong [20] non-isobaric LN_2 evaporation experiments that were carried out over a narrow pressure range (100-145 kPa) in Supplementary Material SM2. The average absolute deviations between both models were less than 1% for all variables, confirming a good performance of the 1-D model.

4 Conclusions

A computationally fast model to predict the non-isobaric evaporation of cryogenic liquids has been developed. It is based on a detailed analysis of the physical phenomena that drive evaporation in storage tanks, using insights obtained from the CFD simulations. The underlying assumption is that wall evaporation and interfacial cooling by liquid natural convection dominate the pressure build-up. The vapour and liquid phases are modelled as 1-D domains in the vertical direction, where heat transfer is governed by a time-dependent heat diffusion equation with volumetric heat sources that account for the heating by the storage tank walls. Additional heat sources are included to allow for the possible condensation of vapour at the interface and for heating of the liquid phase by the bottom of the storage tank. The interface is assumed to be at the saturation temperature, which is a function of the overall pressure. Conjugate heat transfer through the solid tank walls was assumed to lead to evaporation of the cryogen liquid at the interface.

The results of the developed 1-D model were compared with those of the CFD simulations. The 1-D model provides good qualitative agreement with time-dependent vapour and liquid temperature profiles, tank pressure, liquid volume and evaporation rates. In contrast, the neglect of detailed consideration of natural convection leads to overprediction of pressure, resulting in poor prediction of the interface temperature and the vapour temperature profiles. Due to the complexity of non-isobaric cryogen evaporation in storage tanks, even complex CFD and multiphase models require parameter fitting. Considering this limitation, we have used the same experimental data from the literature that we previously used to optimize the CFD model to fit three adjustable parameters in the 1-D model. For this purpose, we used the overall heat transfer coefficients from the surroundings to the vapour and liquid phases, alongside the wall heat partitioning fraction. By optimising the values of these three parameters, the 1-D model recaptured the experimental pressure and the measured temperature profiles with the same accuracy as the CFD model. This demonstrates the usefulness of the 1-D model for practical applications.

The efficiency and simplicity of the 1-D model developed in this work gives it major practical advantages over more complex models. It can simulate several hours of non-isobaric evaporation in less than 10 seconds, making it suitable for model-based control of cryogenic storage tanks, provided that experimental data is used to optimize a small number of heat transfer parameters.

Declaration of Competing Interest

The authors declared that there is no conflict of interest.

CRediT authorship contribution statement

Felipe Huerta: Conceptualisation, Investigation, Methodology, Formal analysis, Software, Writing – original draft. Writing – review and editing. **Ignacio Tapia**: Software, Data Curation, Visualisation. **Velisa Vesovic**: Conceptualisation, Formal analysis, Supervision, Writing – original draft. Writing – review and editing.

Acknowledgments

F. Huerta appreciates the financial support by the project ANID FONDECYT DE INICIACION FOLIO 11241050 of the National Agency of Research and Development (ANID), Chile, and the project ANID/FONDAP /1523A0006 ‘Solar Energy Research Centre’ - SERC – Chile

References

[1] Lee J-S, Cherif A, Yoon H-J, Seo S-K, Bae J-E, Shin H-J, et al. Large-scale overseas transportation of hydrogen: Comparative techno-economic and environmental investigation. Renew Sustain Energy Rev. 2022;165:112556. https://doi.org/10.1016/j.rser.2022.112556.

[2] Yildiz Y, Nalbant M. A review of cryogenic cooling in machining processes. Int J Mach Tools Manuf. 2008;48:947-64. https://doi.org/10.1016/j.ijmachtools.2008.01.008.

[3] Noh Y, Kim J, Kim J, Chang D. Economic evaluation of BOG management systems with LNG cold energy recovery in LNG import terminals considering quantitative assessment of equipment failures. Appl Therm Eng. 2018;143:1034-45. https://doi.org/10.1016/j.applthermaleng.2018.08.029.

[4] Ma G, Lu H, Cui G, Huang K. Multi-stage Rankine cycle (MSRC) model for LNG cold-energy power generation system. Energy. 2018;165:673-88. https://doi.org/10.1016/j.energy.2018.09.203.

[5] Qi M, Park J, Lee I, Moon I. Liquid air as an emerging energy vector towards carbon neutrality: A multi-scale systems perspective. Renew Sustain Energy Rev. 2022;159. https://doi.org/10.1016/j.rser.2022.112201.

[6] Berstad D, Gardarsdottir S, Roussanaly S, Voldsund M, Ishimoto Y, Nekså P. Liquid hydrogen as prospective energy carrier: A brief review and discussion of underlying assumptions applied in value chain analysis. Renew Sustain Energy Rev. 2022;154:111772. https://doi.org/10.1016/j.rser.2021.111772.

[7] Song C, Liu Q, Deng S, Li H, Kitamura Y. Cryogenic-based CO2 capture technologies: State-of-the-art developments and current challenges. Renew Sustain Energy Rev. 2019;101:265-78. https://doi.org/10.1016/j.rser.2018.11.018.

[8] Krikkis RN, Wang B, Niotis S. An analysis of the ballast voyage of an LNG Carrier. The significance of the loading and discharging cycle. Appl Therm Eng. 2021;194:117092. https://doi.org/10.1016/j.applthermaleng.2021.117092.

[9] Migliore C, Tubilleja C, Vesovic V. Weathering prediction model for stored liquefied natural gas (LNG). J Nat Gas Sci Eng. 2015;26:570-80. https://doi.org/10.1016/j.jngse.2015.06.056.

[10] Cryogenic tanks. Linde Engineering; https://www.linde-engineering.com/products-and-services/plant-components/cryogenic-tanks (accessed 17-04-2025)

[11] Fact sheet gas tank: Volvo; 2023. https://stpi.it.volvo.com/STPIFiles/Volvo/FactSheet/LGAS115,%20LGAS155,%20LGAS205_Eng_01_309253877.pdf

[12] Sharafian A, Talebian H, Blomerus P, Herrera O, Mérida W. A review of liquefied natural gas refueling station designs. Renew Sustain Energy Rev. 2017;69:503-13. https://doi.org/10.1016/j.rser.2016.11.186.

[13] Pellegrini LA, Moioli S, Brignoli F, Bellini C. LNG technology: the weathering in above-ground storage tanks. Ind Eng Chem Res. 2014;53:3931-7. https://doi.org/10.1021/ie404128d.

[14] Miana M, Del Hoyo R, Rodrigálvarez V, Valdés JR, Llorens R. Calculation models for prediction of Liquefied Natural Gas (LNG) ageing during ship transportation. Appl Energy. 2010;87:1687-700. https://doi.org/10.1016/j.apenergy.2009.10.023.

[15] Migliore C, Salehi A, Vesovic V. A non-equilibrium approach to modelling the weathering of stored Liquefied Natural Gas (LNG). Energy. 2017;124:684-92. https://doi.org/10.1016/j.energy.2017.02.068.

[16] Sharafian A, Herrera OE, Mérida W. Performance analysis of liquefied natural gas storage tanks in refueling stations. J Nat Gas Sci Eng. 2016;36:496-509. https://doi.org/10.1016/j.jngse.2016.10.062.

[17] Huerta F, Vesovic V. A realistic vapour phase heat transfer model for the weathering of LNG stored in large tanks. Energy. 2019;174:280-91. https://doi.org/10.1016/j.energy.2019.02.174.

[18] Huerta F, Vesovic V. CFD modelling of the isobaric evaporation of cryogenic liquids in storage tanks. Int J Heat Mass Transfer. 2021;176:121419. https://doi.org/10.1016/j.ijheatmasstransfer.2021.121419.

[19] Huerta F, Vesovic V. CryoEvap: An open-source software to simulate the evaporation of cryogenic liquids in vertically orientated storage tanks. SoftwareX. 2025;30:102099. https://doi.org/10.1016/j.softx.2025.102099.

[20] Seo M, Jeong S. Analysis of self-pressurization phenomenon of cryogenic fluid storage tank with thermal diffusion model. Cryogenics. 2010;50:549-55. https://doi.org/10.1016/j.cryogenics.2010.02.021.

[21] Kang M, Kim J, You H, Chang D. Experimental investigation of thermal stratification in cryogenic tanks. Exp Therm Fluid Sci. 2018;96:371-82. https://doi.org/10.1016/j.expthermflusci.2017.12.017.

[22] Perez F, Al Ghafri SZS, Gallagher L, Siahvashi A, Ryu Y, Kim S, et al. Measurements of boil-off gas and stratification in cryogenic liquid nitrogen with implications for the storage and transport of liquefied natural gas. Energy. 2021;222:119853. https://doi.org/10.1016/j.energy.2021.119853.

[23] Al Ghafri SZS, Perez F, Heum Park K, Gallagher L, Warr L, Stroda A, et al. Advanced boil-off gas studies for liquefied natural gas. Appl Therm Eng. 2021;189:116735. https://doi.org/10.1016/j.applthermaleng.2021.116735.
[24] Wan C, Shi C, Zhu S, Fang S, Qiu L, Shi G, et al. Comprehensive design and preliminary experiments of liquid hydrogen storage tank for trucks. Int J Refrig. 2025;169:279-93. https://doi.org/10.1016/j.ijrefrig.2024.10.037.
[25] Gursu S, Sherif SA, Veziroglu TN, Sheffield JW. Analysis and optimization of thermal stratification and self-pressurization effects in liquid-hydrogen storage-systems - Part 1: Model development. J Energy Resour Technol. 1993;115:221-7. https://doi.org/10.1115/1.2905997.
[26] Panzarella C, Kassemi M. One-dimensional model of evaporation and condensation in the presence of a noncondensable gas with applications to cryogenic fluid storage. Int J Heat Mass Transfer. 2009;52:3767-77. https://doi.org/10.1016/j.ijheatmasstransfer.2009.02.027.
[27] Panzarella CH, Kassemi M. Self-pressurization of large spherical cryogenic tanks in space. J Spacecr Rockets. 2005;42:299-308. https://doi.org/10.2514/1.4571.
[28] Panzarella CH, Kassemi M. On the validity of purely thermodynamic descriptions of two-phase cryogenic fluid storage. J Fluid Mech. 2003;484:41-68. https://doi.org/10.1017/s0022112003004002.
[29] Huerta F, Vesovic V. CFD modelling of the non-isobaric evaporation of cryogenic liquids in storage tanks. Appl Energy. 2024;356:122420. https://doi.org/10.1016/j.apenergy.2023.122420.
[30] Hoelzen J, Silberhorn D, Schenke F, Stabenow E, Zill T, Bensmann A, et al. H2-powered aviation – Optimized aircraft and green LH2 supply in air transport networks. Appl Energy. 2025;380. https://doi.org/10.1016/j.apenergy.2024.124999.
[31] Ahluwalia RK, Peng JK, Roh HS, Papadias D, Wang X, Aceves SM. Liquid hydrogen storage system for heavy duty trucks: Capacity, dormancy, refueling, and discharge. Int J Hydrogen Energy. 2023;48:34120-31. https://doi.org/10.1016/j.ijhydene.2023.05.113.
[32] Arnett RW, Voth RO. A computer program for the calculation of thermal stratification and self-pressurization in a liquid hydrogen tank: National Aeronautics and Space Administration; 1972. https://ntrs.nasa.gov/citations/19720016712
[33] Al Ghafri SZS, Swanger A, Jusko V, Siahvashi A, Perez F, Johns ML, et al. Modelling of Liquid Hydrogen Boil-Off. Energies. 2022;15:1149. https://doi.org/10.3390/en15031149.
[34] Krikkis RN. A thermodynamic and heat transfer model for LNG ageing during ship transportation. Towards an efficient boil-off gas management. Cryogenics. 2018;92:76-83. https://doi.org/10.1016/j.cryogenics.2018.04.007.
[35] Zhang Q, Qin B, Xiong Y, Zhou N, Lu Z. Modeling and thermodynamic analysis of liquid carbon dioxide discharge process under backflow-style self-pressurization. Appl Therm Eng. 2025;264:125473. https://doi.org/10.1016/j.applthermaleng.2025.125473.
[36] Al Ghafri SZS, Swanger A, Park KH, Jusko V, Ryu Y, Kim S, et al. Advanced boil-off gas studies of liquefied natural gas used for the space and energy industries. Acta Astronautica. 2022;190:444-54. https://doi.org/10.1016/j.actaastro.2021.10.028.
[37] Ferrín JL, Pérez-Pérez LJ. Numerical simulation of natural convection and boil-off in a small size pressurized LNG storage tank. Comput Chem Eng. 2020;138:106840. https://doi.org/10.1016/j.compchemeng.2020.106840.
[38] Saleem A, Farooq S, Karimi IA, Banerjee R. A CFD simulation study of boiling mechanism and BOG generation in a full-scale LNG storage tank. Comput Chem Eng. 2018;115:112-20. https://doi.org/10.1016/j.compchemeng.2018.04.003.
[39] Huerta F, Vesovic V. Analytical solutions for the isobaric evaporation of pure cryogens in storage tanks. Int J Heat Mass Transfer. 2019;143:118536. https://doi.org/10.1016/j.ijheatmasstransfer.2019.118536.
[40] Tatom JW, Brown WH, Knight LH, Coxe EF. Analysis of Thermal Stratification of Liquid Hydrogen in Rocket Propellant Tanks. In: Timmerhaus KD, editor. Advances in Cryogenic Engineering. Boston, MA: Springer US; 1964. p. 265-72.https://doi.org/10.1007/978-1-4757-0525-6_31.
[41] Schmidt AF, Purcell JR, Wilson WA, Smith RV. An Experimental Study Concerning the Pressurization and Stratification of Liquid Hydrogen. J Res Natl Bur Stand. 1960:487-97. https://doi.org/10.1007/978-1-4757-0537-9_56.
[42] Ren J, Zhang H, Bi M, Yu J, Sun S. Numerical investigation of the coupled heat transfer of liquefied gas storage tanks. Int J Hydrogen Energy. 2017;42:24222-8. https://doi.org/10.1016/j.ijhydene.2017.07.155.
[43] Ren J, Zhang H, Yu J, Bi M, Sun S. Experimental research of heat-mass coupling response of liquid storage tanks. J Hazard Mater. 2017;338:502-7. https://doi.org/10.1016/j.jhazmat.2017.05.060.
[44] Schiesser WE, Griffiths GW. A compendium of partial differential equation models: method of lines analysis with Matlab. 1st ed. Cambridge ; New York: Cambridge University Press; 2009.https://doi.org/10.1017/CBO9780511576270.

[45] Shampine LF. Solving 0 = F(t, y(t), y'(t)) in Matlab. J Numer Math. 2002;10:291-310. https://doi.org/10.1515/JNMA.2002.291.
[46] Span R, Lemmon EW, Jacobsen RT, Wagner W, Yokozeki A. A Reference Equation of State for the Thermodynamic Properties of Nitrogen for Temperatures from 63.151 to 1000 K and Pressures to 2200 MPa. J Phys Chem Ref Data. 2000;29:1361-433. https://doi.org/10.1021/ie4033999.
[47] Bell IH, Wronski J, Quoilin S, Lemort V. Pure and pseudo-pure fluid thermophysical property evaluation and the open-source thermophysical property library CoolProp. Ind Eng Chem Res. 2014;53:2498-508. https://doi.org/10.1021/ie4033999.
[48] Hasan MM, Lin CS, Vandresar NT. Self-pressurization of a flightweight liquid hydrogen storage tank subjected to low heat flux. NASA Technical Memorandum 103804. Minneapolis, Minnesota.1991. https://ntrs.nasa.gov/citations/19910011011